This is a preprint, the final version is subject to change, of the American Mineralogist (MSA)
Cite as Authors (Year) Title. American Mineralogist, in press.
(DOI will not work until issue is live.) DOI: http://dx.doi.org/10.2138/am-2016-5706

Revision 2

Growth of hydrothermal baddeleyite and zircon in different stages of skarnization

Wen Winston Zhao[1], Mei-Fu Zhou[1*], and Wei Terry Chen[2]

1 Department of Earth Sciences, The University of Hong Kong, Pokfulam Road, Hong Kong, China

2 State Key Laboratory of Ore Deposit Geochemistry, Institute of Geochemistry, Chinese Academy of Sciences, Guiyang 550002, China

---

E-mail address:

Wen Winston Zhao: *zhaowen@hku.hk*; +852-56133681

Mei-Fu Zhou: *mfzhou@hku.hk*; +852-28578251 (*corresponding author)

Wei Terry Chen: *chenwei@mail.gyig.ac.cn*; +86-13710113486

ABSTRACT

Both prograde and retrograde skarns from the Tengtie iron deposit, South China contain rounded, euhedral, and anhedral zircon grains. Rounded grains were originally derived from detritus in carbonate rocks and were incorporated into the skarns. Euhedral and anhedral crystals are intergrown with various skarn minerals and are clearly hydrothermal in origin. These hydrothermal grains have low $(Sm/La)_N$ ratios and high La contents relative to typical magmatic ones and display flat LREE and subdued flattening of HREE chondrite-normalized patterns, similar to those of zircon crystallized from Zr-saturated fluids. Prograde skarns also contain baddeleyite rimed by zircon, which record a period of low Si activity during prograde skarnization relative to original magmatic-hydrothermal fluids. Hydrothermal zircon grains from Tengtie have variable Eu anomalies and slightly positive Ce anomalies, indicating that they may have crystallized from highly heterogeneous, but generally reducing fluids. They have low $\delta^{18}O$ values (-5.1 to -2.7 ‰), suggesting the involvement of meteoric fluids. Fluorine-rich fluids played an important role in remobilizing and transporting some high field strength elements (HFSE), including Zr, from the host granites into the skarn system. Reaction between HFSE-bearing fluids and carbonate rocks at the prograde stage decomposed F complexes to deposit HFSE-rich skarn minerals and baddeleyite. At the retrograde stage, alteration of the HFSE-rich skarn minerals released HFSE, including Zr and Sn, consequently producing a mineral assemblage of zircon, cassiterite, and retrograde skarn minerals. Dating results of zircons from the Tengtie skarn system by SIMS indicates roughly less than several million years duration for skarnization. Our study indicates that Zr was not

45 only mobile locally under favorable conditions, but was also readily transported and
46 deposited in different stages of skarnization.
47
48 **Keywords**: baddeleyite, zircon, oxygen isotope, U-Pb geochronology, skarnization,
49 HFSE
50

INTRODUCTION

Being one of the high field strength elements (HFSE), zirconium (Zr) has long been considered to be immobile during metamorphism or alteration (e.g., Ague 1994; Bebout et al. 1999; Ague 2003; Breeding et al. 2004; Penniston-Dorland and Ferry 2008; Ague 2011), and is widely used for petrogenetic studies (e.g., Pearce and Cann 1973; Floyd and Winchester 1975; Drummond et al. 1996; Pearce 1996; Solar and Brown 2001; Ernst and Buchan 2003; Pearce 2008). However, an increasing body of evidence has shown that Zr can be mobilized by hydrothermal fluids and re-deposited as hydrothermal Zr-bearing minerals (e.g., Kerrich and King 1993; Nesbitt et al. 1999; Hoskin 2005; Pettke et al. 2005; Geisler et al. 2007; Lawrie et al. 2007; Pelleter et al. 2007; Kusiak et al. 2009; Toscano et al. 2014; Deng et al. 2015).

Skarns typically exhibit a temporal evolution with early-formed high temperature phases precipitated from magmatic fluids overprinting isochemical thermal metamorphic marble and hornfels, in turn variably replaced by late low temperature assemblages involved in meteoric and/or basinal fluids (Einaudi et al. 1981; Meinert et al. 2005; Rubenach 2013). Some studies have reported hydrothermal Zr-bearing minerals in contact zones between igneous rocks and carbonate sedimentary rocks (e.g., Gieré 1986; Rubin et al. 1989; Gieré and Williams 1992; Rubin et al. 1993; Moine et al. 1998; Deng et al. 2015). Specifically, hydrothermal zircons in these skarns show a variety of morphologies, and sometimes contain skarn mineral inclusions (e.g., Rubin et al. 1989; Deng et al. 2015). Furthermore, Rubin et al. (1993) proposed that leaching of igneous source rocks by F-rich hydrothermal fluids could be the major control on the precipitation of zircon in associated skarn assemblages. Recently, Deng et al. (2015) analyzed

hydrothermal zircon by LA-ICP-MS showing a genetic relationship between iron skarn mineralization and the coeval magmatism. However, it remains unclear whether Zr-bearing minerals can form during different stages of skarnization, and what controls the growth of these minerals corresponding to the skarnization. Moreover, understanding the formation of Zr-bearing minerals in skarns can place significant constraints on the mechanism of mobilization, transportation, and deposition of Zr, and the fluid evolution of skarn systems, not only because of their presence, but also because they would be precisely dated using the U-Pb isotopic system to place tight temporal constraints on the timing of the ore-forming hydrothermal system if enough high precision of techniques were achieved.

Here, we report findings of hydrothermal baddeleyite and zircon in mineralized skarns from the Tengtie iron deposit, South China. Their textural relationships with other skarn minerals, and elemental and oxygen isotopic compositions indicate their formation in both the prograde and retrograde stages of skarnization. The results lead us to conclude that Zr was mobilized from granitic rocks by F-bearing hydrothermal fluids and that the formation of hydrothermal baddeleyite and zircon under different physical and chemical conditions protracted mineralization in the deposit. In addition, dating the magmatic zircon and skarn zircon provides important constraints on the duration of skarnization.

GEOLOGICAL SETTING AND SAMPLING

The present tectonic framework of South China was produced by multiple collisions of lithospheric blocks, and formed the South China Block, which is further divided by the northeast-southwest-trending Jiangshan-Shaoxing Suture (J-S Suture) into the Yangtze

Block in the northwest and the Cathaysia Block in the southeast (Fig. 1a) (Zhao et al. 2011). The Yangtze Block is composed of Archean to Paleoproterozoic crystalline basement overlain by Neoproterozoic to Cenozoic sedimentary strata (Zhou et al. 2002; Yan et al. 2003). The Cathaysia Block is made up of Precambrian basement covered by the Neoproterozoic to Meosozoic sedimentary and volcanic sequences (Chen and Jahn 1998; Yu et al. 2005). The whole Cathaysia Block and the eastern part of the Yangtze Block witnessed an extensive Mesozoic igneous event, divided into the early (180-142 Ma) and late (140-66 Ma) phases, which were related to the subduction of paleo-Pacific plate (Zhou et al. 2006). Numerous deposits in the Nanling Range of the central part of South China are genetically related to this event (Hu and Zhou 2012; Mao et al. 2013).

The Tengtie iron skarn deposit in the southern Nanling Range occurs along the contact zone between the Devonian to Carboniferous strata and the Mesozoic granitic pluton (Fig. 1b). Devonian to Carboniferous strata are made up of dolomite and dolomitic limestone with sandstone and siltstone, and the carbonate layers are the main magnetite ore host. Early barren Sinian to Cambrian strata are composed of low-grade metamorphosed clastic rocks locally interbedded with carbonates (Zhao and Zhou 2015). The Mesozoic pluton is composed of early porphyritic (144.3 ± 0.8 Ma) and late fine-grained (106.4 ± 0.7 Ma) biotite granite as products of partial melting of the Mesoproterozoic continental crust under an extension tectonic setting (Gao et al. 2005). To the northwest, the Silurian pluton is granodiorite with an age of 419.1 ± 6.4 Ma, which was formed by partial melting of lower crust metasedimentary rocks with participation of mantle materials (Cheng et al. 2009). Ore bodies in this deposit are distributed in several mining districts, and aeromagnetic anomalies have been detected as

120 areas for additional prospecting (Fig. 1b). The estimated ore reserves of the deposit
121 include 72 Mt iron and 0.6 Mt non-ferrous metals (e.g., W, Mo, and Au), which together
122 constitute one of the important Fe skarn deposits in South China (Zhao and Zhou 2015).

123 Massive and disseminated skarn ores are dominated by magnetite with variable
124 amounts of chalcopyrite, pyrite, sphalerite, galena, and cassiterite. The paragenetic
125 sequence shows early prograde and retrograde stages of silicate and oxide minerals, and a
126 late sulfide stage of pyrite, shpalerite, galena, and chalcopyrite (Zhao and Zhou 2015).
127 The prograde stage is characterized by diopsidic pyroxene, andraditic garnet, and humite,
128 with accessary zircon, baddeleyite, fluorite, and apatite. The retrograde stage contains
129 phlogopite, chlorite, epidote, quartz, and calcite, with minor amounts of zircon and
130 cassiterite. The late retrograde stage is also accompanied by magnetite formation.

131 More than one hundred samples of skarns and granites were collected from
132 underground workings in the Tengtie (24º07′ N, 112º13′ E) and Dongyuan (24º08′ N,
133 112º20′ E) mining districts, as well as the fresh surface outcrop. Twenty samples were
134 selected for zircon observation and separation. Early porphyritic biotite granite samples
135 are TT14-13 from the underground working of the Tengtie mining district (~100 m away
136 from the skarn contact), and LY14-35 (24º16′ N, 112º08′ E), LY14-45 (24º16′ N, 112º08′
137 E), LY14-54 (24º14′ N, 112º08′ E), and GD1228 (24º12′ N, 112º09′ E) from the fresh
138 surface outcrop. They are composed of quartz (25-40 vol%), alkaline-feldspar (30-45
139 vol%), plagioclase (15-25 vol%), and biotite (~5 vol%), with accessory zircon, magnetite,
140 titanite, and apatite. Late fine-grained biotite granite samples are TT14-1617 and TT14-
141 34 from the underground working of the Tengtie mining district (~90 m away from the
142 skarn contact), and LY14-1617 (24º16′ N, 112º08′ E), LY14-34 (24º16′ N, 112º08′ E),

and GD1227 (24º18′ N, 112º08′ E) from the fresh surface outcrop. They consist of quartz (30-35 vol%), alkaline-feldspar (35-45 vol%), plagioclase (20-30 vol%), and biotite (~5 vol%), with accessory minerals of zircon, apatite, titanite, and magnetite. Skarn samples are all exoskarn from the Tengtie (TT14-02, TT14-0203, TT14-04, TT14-05, TT14-117, F01, F02, F03, and F04) and Dongyuan (DY02) mining districts. They are composed of diopside (50-90 vol%), andratitic garnet (0-20 vol%), magnetite (0-30 vol%), epidote (0-20 vol%), chlorite (0-20 vol%), tremolite (0-10 vol%), and calcite (0-10 vol%), and quartz (0-5 vol%), with minor amounts of zircon, fluorite, and apatite.

ANALYTICAL TECHNIQUES

Hand specimens were sawed into rock chips for preparation of mineral separates and thin sections, respectively. Zircons were separated from ten granite samples (TT14-1617, TT14-34, TT14-13, LY14-1617, LY14-34, LY14-35, LY14-45, LY14-54, GD1227, and GD1228) and three skarn samples (TT14-05, TT14-117, and TT14-0203), using standard density and magnetic separation techniques. Zircon grains, together with zircon U-Pb and oxygen isotope standards (Qinghu, Penglai and Plésovice), were cast in epoxy grain mounts, which was then polished to section the crystals in half for analysis. Uncoated thin sections and mounts were documented using transmitted and reflected light micrographs, and then scanning electron microscopy (SEM) at the Electron Microscope Unit, The University of Hong Kong (HKU). Selected sections and mounts were further vacuum-coated with high-purity gold and carbon, respectively, for Cathodoluminescence (CL) imaging at the Department of Earth Sciences, HKU, and electron microprobe (EMP) analyses at the State Key Laboratory of Continental Tectonics and Dynamics, Chinese

Academy of Geological Sciences, Beijing. Gold-coated zircon mount samples (TT14-05, TT14-117, LY14-1617, LY14-34, LY14-35, LY14-45, and LY14-54) were then used for U-Th-Pb and oxygen isotopic analyses (Li et al. 2009; Li et al. 2010; Tang et al. 2015) at the Institute of Geology and Geophysics, Chinese Academy of Sciences, Beijing. Re-polished sections (DY02, F02, TT14-04, and TT14-02) and mount samples (GD1227 and GD1228) were used for *in-situ* trace element analyses by laser ablation ion coupled plasma mass spectrometry (LA-ICP-MS) for zircon (Liu et al. 2010) at the State Key Laboratory of Geological Processes and Mineral Resources, China University of Geosciences, Wuhan, and for clinopyroxene and garnet (He et al. 2015) at the Chinese Academy of Sciences Key Laboratory of Crust-Mantle Materials and Environments, University of Sciences and Technology of China, Hefei. Four fluid inclusion sections (F01, F02, F03, and F04) were made for microthermometry studies of calcite from the retrograde skarn stages at the Guangzhou Institute of Geochemistry, Chinese Academy of Sciences, Guangzhou. Details regarding the analytical techniques above are provided in the Supplementary Appendix.

PETROGRAPHY OF ZIRCON

Four types of zircon (Type 1, Type 2, Type 3, and Type 4) were recognized based on their occurrences and morphologies (Figs. 2-3; Supplementary Figures). Type 1 and Type 2 zircons, sampled from skarns in the Tengtie and Dongyuan districts, are all transparent. Type 1 zircon is further subdivided into Type 1a and Type 1b for prograde and retrograde skarn assemblages, respectively. Type 1a zircon from the prograde skarns is always as anhedral rims around anhedral baddeleyite with sharp contacts, and usually less than 15

μm in size (Figs. 2a-b; Supplementary Figure S1). The baddeleyite and zircon, accompanied by apatite and fluorite, always occur in the pores of the prograde skarn minerals (e.g., diopside). Type 1b zircon from the retrograde skarns ranges in size from nanometers to more than 100 μm, but most are less than 30 μm across (Figs. 2c-d; Supplementary Figures S2-3). Large grains of Type 1b are euhedral or subhedral associated with cassiterite, calcite, epidote, and chlorite with curved or straight contacts. Some of these grains contain epidote or calcite inclusions. Tiny-size Type 1b is usually needle-like along the cleavages of the chlorite (Fig. 2e). Both the large and small Type 1b grains are associated with magnetite mineralization in the retrograde skarns (Fig. 2f). Under CL, a zonation pattern is seen in which individual zones appear to be wide and faint (Fig. 2g). Two-phase fluid inclusions, about 5 μm in diameter, occur in large, euhedral Type 1b zircon grains (Fig. 2h). Type 2 zircon from skarns is usually rounded, which is obviously different from Type 1 (Figs. 3a-d; Supplementary Figure S4). They are about 30 μm in width, and often have a dark faint zoning inner core with white homogeneous rims under CL. Typically, most grains of this type are free of inclusions.

Type 3 zircon from the late fine-grained biotite granite and Type 4 zircon from the early porphyritic biotite granite are transparent and translucent (Fig. 3; Supplementary Figure S4), respectively. Transparent Type 3 zircon grains are mostly euhedral with a size of around 200 μm and typical magmatic oscillatory zoning (Fig. 3f), and contain apatite inclusions (Fig. 3e). In contrast, translucent Type 4 zircon is usually larger than 200 μm, and shows complex textures under BSE and CL imaging, which generally consists of dark and bright domains with a sharp interface (Figs. 3i-j). The BSE-dark domains typically contain pores and inclusions of HFSE-rich minerals (e.g., thorite),

whereas the BSE-bright parts are mostly free of inclusions. Under CL images, the BSE-dark parts are black with no visible textures, whereas the BSE-bright parts have weak zoning with narrow bands. Fractured and porous textures are common in the translucent zircon grains (Fig. 3i).

ANALYTICAL RESULTS

Type 1 zircons from skarns and transparent Type 3 zircons from the late fine-grained granite have similar major element compositions, different from those of the translucent Type 4 zircons in the early porphyritic granite, which typically have distinctly lower ZrO_2 (48.8 to 56.8 wt%), slightly lower SiO_2 (29.2 to 32.5 wt%), and higher U (4.07 to 8.04 wt%) and Hf (1.42 to 3.03 wt%) (Table 1). The relatively low oxides totals (95.02 to 97.71 wt%) of the translucent zircons may be due to the incorporation of a hydrous component in the radiation-damaged structure (Nasdala et al. 2001) or the porous surface as mentioned earlier. Specifically, the BSE-bright domains of the translucent Type 4 zircons have relatively high Zr and low U concentrations compared to the BSE-dark domains of these grains, but the Si and Hf concentrations do not show apparent variations in a single grain under X-Ray elemental mappings (Figs. 3m-p).

In the skarns, the Type 1b zircons have $\delta^{18}O$ values (-5.1 to -2.7 ‰) much lower than the rounded Type 2 zircon grains (5.0 to 12.0 ‰). Transparent Type 3 zircon grains from the late fine-grained biotite granite have $\delta^{18}O$ values (5.8 to 7.7 ‰) similar to those of typical magmatic zircon (e.g., Valley 2003). The $\delta^{18}O$ values of inclusion- and crack-free domains in the translucent Type 4 zircons from the early porphyritic biotite granite are roughly similar, ranging from 5.2 to 7.9 ‰ with a peak slightly lower than that of the

transparent Type 3 zircon (Fig. 4 and Supplementary Table S1). However, due to metamictization or possible later hydrothermal alteration, the $\delta^{18}O$ values of the translucent high-U Type 4 zircons could not represent the primary signature. However, the narrow $\delta^{18}O$ ranges indicate that the different matrix effects would have less impact on the analyses, but the later potential homogeneous hydrothermal fluids might play a more important role (e.g., Wang et al. 2014).

The low U content of zircon is more suitable for SIMS U-Pb dating than high U zircons, because extremely high U may cause intense metamictization leading to matrix effects on SIMS analyses (White and Ireland 2012; Pidgeon et al. 2013; Wang et al. 2014). Analyses of Type 3 and Type 1b zircons yield concordia ages of 99.3 ± 0.5 Ma (N=9; MSWD=0.0004) and 97.5 ± 0.7 Ma (N=5; MSWD=5.2), respectively (Figs. 5a and c). However, the rounded zircons from the skarn have a wide range of ages with the youngest $^{206}Pb/^{238}U$ age at 416.2 ± 7.1 Ma, and some points plotting off concordia (Fig. 5b). Dating of high U radiation damaged zircon provide dispersed unreal ages ($^{206}Pb/^{238}U$ ages from 88.7 ± 1.3 Ma to 137.3 ± 2.1 Ma; Supplementary Table S2) younger or older than the unknown real age (e.g., Wang et al. 2014).

The translucent Type 4 zircons have total concentrations of REE (7039–14259 ppm) much higher than the transparent Type 3 zircons (550–1758 ppm) and Type 1b zircons (58–143 ppm) (Supplementary Table S3). The transparent zircons have more pronounced positive Ce anomalies (Ce/Ce^{*}=11–156) than the translucent (1–6) and irregular (3–15) grains (Fig. 6). The Type 1b zircons have variable Eu anomalies (Eu/Eu^{*}: 0.16–1.48), whereas all the zircons from the granites have significantly negative Eu anomalies (Fig. 6).

Based on the core-rim texture in different mineral assemblages and major element variations (e.g., Einaudi et al. 1981; Meinert et al. 2005), diopside and andratitic garnet from early prograde and late prograde assemblages were distinguished and show distinct trace elemental compositions (Supplementary Table S4). In the prograde skarn stages, the water/rock ratios was high, and thus the partitioning of trace elements in the prograde skarn minerals would be mainly buffered by the fluid compositions (Gaspar et al. 2008). The early prograde skarn minerals are enriched in HFSE with respect to the late prograde skarn minerals (e.g., Ti, Zr, Nb, Sn, and REE) (Fig. 7). Also, it is remarkable that skarn minerals from both early and late prograde stages are typically enriched in light rare earth elements (LREE) relative to heavy rare earth elements (HREE).

Calcite grains in the retrograde skarns coexisting with the Type 1b zircon grains contain two-phase fluid inclusions, ranging from 5 to 15 μm, which are similar to those in hydrothermal zircon grains (Fig. 3h). Homogenization temperatures of these fluid inclusions in associated calcite range from ~330 to ~230 ºC (Fig. 8). Salinity of these aqueous fluid inclusion, estimated using the data of Bodnar (1994) for the NaCl-H_2O system, ranges from 6.6 to 17.5 wt% NaCl equiv.

DISCUSSION

Baddeleyite and zircon in skarn systems

Zircon grains from the Tengtie skarns have a variety of morphologies and chemical compositions indicating different origins. The Type 2 zircon grains, with their well-rounded edges, are unlikely to have grown *in situ* in the skarn. Indeed, they have wide variations of oxygen isotope values (5.0 to 12.0 ‰) (Fig. 4b), consistent with their

281 diverse origins. Considering that the host Devonian strata in the region are interpreted to
282 have formed in a platform-basin system (Chen et al. 2001), which may have various
283 terrestrial sources, the Type 2 grains are interpreted as detrital in origin. Such an
284 interpretation is also supported by the wide range of their ages, which are concentrated
285 between ~1.7 to ~1.9 Ga with the youngest age of ~416 Ma (Fig. 5b). These age
286 distributions indicate that the major contributor to the sedimentary detritus could be
287 Paleoproterzoic sources in South China with minor contributions from Caledonian
288 sources, such as the Silurian pluton in this region.

289 In contrast, the Type 1 zircon grains, including euhedral and anhedral ones, are
290 unlikely to be detrital in origin, because their ages of ~98 Ma are much younger than
291 those of the strata (Fig. 5a). The close association of the hydrothermal baddeleyite and
292 zircon with different skarn minerals indicates that the zircon has grown during different
293 stages of skarnization, and thus is hydrothermal in origin (e.g., Deng et al. 2015). Such an
294 interpretation is further supported by the presence of two-phase fluid inclusions in the
295 Type 1 zircon grains, a feature that is similar to hydrothermal zircons formed in some
296 high-sulphidation Au–Ag–(Cu) deposits (Lawrie et al. 2007) and skarn Fe deposits in
297 North China (Deng et al. 2015). In addition, Type 1 zircons have high La contents and
298 low $(Sm/La)_N$ values relative to magmatic ones and display flat LREE and gently
299 positively sloping HREE patterns (Fig. 6), typical of zircon precipitated from
300 hydrothermal fluids (e.g., Hoskin 2005; Pelleter et al. 2007; Kirkland et al. 2009).

301 In the prograde skarns, anhedral baddeleyite, rimmed by Type 1a zircon, is present
302 in interstitial pores of the prograde skarn minerals (e.g., diopside) (Fig. 2a). It is noted
303 that such zircon-bearing pores do not contain any retrograde minerals, different from the

304 pores that suffered from retrograde alteration. This feature thus indicates that the
305 formation of both the baddeleyite and Type 1a zircon might slightly postdate the
306 prograde skarn minerals, and should be products of prograde skarnization. The
307 baddeleyite-zircon association is not common in skarns. The most plausible explanation
308 is that during the skarnization, baddeleyite might crystallize firstly from relatively low Si-
309 bearing fluids. Subsequent incursion of the SiO_2-rich hydrothermal fluids partially altered
310 it to form zircon rims during successive periods of skarn alteration, in response to the
311 increase of silica activity (e.g., Davidson and Van Breemen 1988). Such a phenomenon is
312 also common in metamorphosed mafic dykes during the initial stages of metamorphism,
313 where baddeleyite can decompose to a polycrystalline zircon via the reaction: ZrO_2 +
314 $SiO_2 = ZrSiO_4$ (Davidson and Van Breemen 1988; Söderlund et al. 2008).

315 Similarly, in the retrograde skarns, hydrothermal Type 1b zircons are closely
316 associated with the retrograde skarn minerals. Some of them contain inclusions of
317 minerals identical to those from the retrograde skarns (Figs. 2c-d), and some occur as
318 intergrowth in the cleavages of chlorite (Fig. 2e). These features indicate that both the
319 zircon and retrograde skarn minerals precipitated at the same time. Therefore,
320 hydrothermal zircon must have formed during the retrograde stages of skarnization.

321 In general, Zr in hydrothermal fluids, which results in the formation of
322 hydrothermal baddeleyite and zircon in skarns, can potentially be sourced by local
323 remobilization of Zr or transported from external sources by fluids. A potential local
324 source of Zr might be the detrital Type 2 zircons. However, no evidence of dissolution on
325 the rounded Type 2 zircon surfaces was seen. Localized minor cracks in this type of
326 zircon could have been created during mineral separating processes (Figs. 3a-d;

Supplementary Figure S4). In addition, the low U contents in Type 2 zircons would not allow for much radiation damage of the crystallographic lattice, which, if it occurred, would enhance dissolution and recrystallization (e.g., Geisler et al. 2001; Dempster et al. 2004). This would argue against the possibility of local remobilization of detrital zircon grains during much later hydrothermal events. Thus, the Zr in the fluids was likely derived from external sources. It is suggested that during skarnization, both early magmatic-hydrothermal and late meteoric-hydrothermal fluids can leach and transport components from external sources (Meinert et al. 2005). The occurrence of hydrothermal baddeleyite and zircon in the prograde skarns at Tengtie suggests that Zr was probably transported into the skarn system at the beginning of skarnization. Indeed, the high water/rock ratios, present during early prograde skarnization, imposed pronounced HFSE concentrations on diopside and garnet, especially Zr and Sn (Fig. 7), implying that the magmatic-hydrothermal fluids, which evolved from the granitic magmas, were already enriched in HFSE (e.g., Smith et al. 2004; Gaspar et al. 2008; Ismail et al. 2014).

Alternatively, modification of zircon is well recorded in the radiation-damaged domains of the translucent zircons from the early phase of the Mesozoic pluton (Figs. 3i-l). Such a feature is similar to the experimental results of Geisler et al. (2007). Hence, it seems that Zr could be sourced from such mobilization processes. However, this possibility is excluded by the general acceptance that alteration of high-U zircon usually occurs after the crystal structure is damaged by radiation, which takes at least several millions of years under low temperature (e.g., Mezger and Krogstad 1997; Geisler et al. 2003). Also, it has been demonstrated in several studies (e.g., Mursic et al. 1992; McLaren et al. 1994; Mezger and Krogstad 1997; Rizvanova et al. 2000) that metamict

zircon can recover their crystallinity rapidly under the laboratory condition above about 600 ºC. During the latter stages of granitic crystallization, magmatic-hydrothermal fluids evolved from residual melts would generally be around 650 ºC (Einaudi et al. 1981; Meinert et al. 2005). As such, it is possible that the initially radiation damaged high U, Type 4 zircon in the Mesozoic pluton had already recrystallized when the late granitic phase was intruding. This is further supported by the fact that the early high U, Type 4 cores are present in the late Type 3 zircons from the late granitic phase (Supplementary Figure S4). The Type 3 zircons have a SIMS age of 99.3 ± 0.5 Ma, comparable to that of the hydrothermal Type 1b zircon (97.5 ± 0.7 Ma). Therefore, the annealing and leaching processes experienced by the high U, Type 4 zircon might not correspond to the main, high temperature skarnization event. Overall, the Zr source for the hydrothermal baddeleyite and zircon, during different stages of skarnization, most likely was from the late intrusive phase of the Mesozoic granitic pluton.

Nature of hydrothermal fluids

The association of the hydrothermal zircon with fluorite in the skarns implies that F-rich fluids were most likely responsible for the mobilization and transportation of Zr as $ZrF_n(OH)_m^0$ (c.f., Salvi and Williams-Jones 1996; Salvi et al. 2000; Migdisov et al. 2011). It is generally accepted that REEs can form stable highly mobile, complexes with both fluoride and chloride anions (e.g., Haas et al. 1995; Migdisov and Williams-Jones 2007; Migdisov et al. 2009; Tropper et al. 2011; Tropper et al. 2013). However, while REE chlorides are relatively soluble at moderate temperatures (~300 to ~500 ºC), REE fluorides are relatively insoluble at these temperatures, which limits the amount of REEs

373 transported as REE fluoride complexes (Williams-Jones et al. 2012; Williams-Jones and
374 Migdisov 2014). As such, the hydrothermal Type 1b zircons deposited from such F-rich
375 fluids have the lowest REE contents compared to the other zircon grain types (Fig. 6).
376 Notably, the different degrees of enrichment of LREE in the prograde diopside and
377 andraditic garnet (Fig. 7) is in agreement with the relatively high mobility of LREE in F-
378 rich fluids compared to HREE (excluding Y, which here is strongly partitioned into
379 garnet) (e.g., Migdisov et al. 2009; Williams-Jones et al. 2012; Linnen et al. 2014;
380 Williams-Jones and Migdisov 2014). Hence, we propose that the F-rich, magmatic-
381 hydrothermal fluids were evolved from the late granitic magmas, with the REE
382 (LREE>HREE) and HFSE, interacting with the carbonates to form skarns.
383 Cerium anomalies of in zircon are likely related to the oxidation state of the fluids
384 (Trail et al. 2011), whereas Eu anomalies are more likely related to the REE chemistry of
385 the fluids rather than the redox conditions (Pelleter et al. 2007). Variable Eu anomalies in
386 Type 1b zircons from the Tengtie retrograde skarns indicate that the fluids were spatially
387 compositionally heterogeneous, whereas the generally low Ce anomalies suggest low-
388 temperature, reducing fluids relative to those precipitating the Type 3 zircons (e.g., Trail
389 et al. 2011). Such a relatively reducing environment is also indicated by the formation of
390 magnetite rather than hematite during the retrograde skarnization (Fig. 2f). The relatively
391 low temperature and reducing affinities of the retrograde heterogeneous fluids might have
392 resulted from the different degrees of mixture between the magmatic and meteoric fluids
393 in different places during retrograde skarnization. Such an interpretation is supported by
394 the oxygen isotopic composition of the Type 1b zircon. The fluid inclusions in calcite,
395 coexisting with the zircon, have homogenization temperatures around of 300 ºC (Fig. 8),

similar to that reported in slate (Dempster et al. 2004) and high sulfidation deposits (Lawrie et al. 2007). This fluid has a moderate salinity (6.6-17.5 wt% NaCl equiv.). Using this temperature of 300 ºC, the oxygen isotopic ratios of the zircon, and corresponding information from Zheng (1993), we calculate $\delta^{18}O$ values of -3.28 to -0.89 ‰ for the retrograde hydrothermal fluids, which is consistent with the mixing sources involving magmatic and meteoric fluids.

Formation of baddeleyite and zircon during skarnization

Formation of skarns is a dynamic process, involving different hydrothermal stages and a continuous fluid evolution process (Meinert et al. 2005). Our findings in this study clearly provide clues on the mobilization of Zr during skarnization and subsequent formation of baddeleyite and zircon in skarns.

The Mesozoic pluton associated with the Tengtie skarn deposit was derived from the partial melting of Mesoproterozoic continental crust in South China under the tectonic setting of subduction of the paleo-Pacific plate (Gao et al. 2005). The late fine-grained biotite granite intruded into the Neoproterozoic and Paleozoic strata at 99.3 ± 0.5 Ma (Fig. 5c). In granitic melts, Zr is controlled primarily by zircon, and zircon solubility increases strongly with increasing F (Keppler 1993; Linnen et al. 2014). Incompatible elements, such as Zr and REE, could prefer to concentrate in the fluid-rich residual melt from which the subsolvus granite formed (e.g., Yang et al. 2014). Therefore, in Tengtie, F-rich magmatic-hydrothermal fluids (> 650 ºC) could have been directly derived from evolved magmas of this granitic phase by magma boiling (Fig. 9a). Such relatively high-temperatures and oxidizing fluids would have contained elevated Zr as $ZrF_n(OH)_m^0$,

419 along with Si, Sn, and some other HSFE. Once the internal hydrostatic pressure became
420 larger than the lithostatic pressure, hydrofracturing was triggered, resulting in the
421 penetration of magmatic-hydrothermal fluids along extensive fractures in the country
422 rocks (e.g., Einaudi et al. 1981; Ciobanu and Cook 2004; Meinert et al. 2005).

423 At the beginning of skarnization, the Zr-bearing fluids interacted with the
424 surrounding carbonates to produce prograde skarn minerals (e.g., early diopside),
425 consuming Si with some Zr, Sn, and other HFSE (Fig. 9b), during which porosity in the
426 country rocks was enhanced. Shortly after the deposition of early diopside, Ca activities
427 in the skarn systems were probably still high such that $ZrF_n(OH)_m^0$ broke down to
428 baddeleyite accompanied by fluorite (Fig. 2b) (e.g., Salvi et al. 2000). Notably, the
429 occurrence of baddeleyite in the prograde skarns suggests that during the formation of the
430 early prograde skarn minerals, the fluids were relatively depleted in Si relative to original
431 magmatic-hydrothermal fluids but oversaturated in Zr. Subsequent increase of Si activity,
432 due to continuous input of relatively Si-rich magmatic-hydrothermal fluids, resulted in
433 the decomposition of baddeleyite into the Type 1a zircon rims as observed (Fig. 9c).

434 Retrograde skarnization was related to the evolved fluids that were depleted in
435 HFSE relative to the prograde fluids. The retrograde skarnization was characterized by
436 alteration of prograde minerals to retrograde minerals (Meinert et al. 2005), during which
437 Zr and Sn with Si in the early prograde skarn minerals (e.g., diopside and garnet), were
438 released into the fluids. The released Zr and Sn were responsible for the formation of
439 cassiterite and Type 1b zircon (97.5 ± 0.7 Ma; Fig. 5a) together with retrograde skarn
440 minerals, such as chlorite, epidote, and calcite (Figs. 2c-f). Meteoric-hydrothermal fluids
441 must have been involved in the retrograde process, as suggested by the low $\delta^{18}O$ of the

hydrothermal Type 1b zircon (-5.1 to -2.7 ‰) (e.g., Cavosie et al. 2005; Kirkland et al. 2009). Finally, hydrothermal Type 1b zircon grains in Tengtie skarns were deposited in a low-temperature (< 400 ºC) reducing fluid system (Fig. 9d). SIMS dating suggests that the duration of this entire process, from the intrusion of late granitic phase to deposition of retrograde hydrothermal zircon, was less than several million years, which is consistent with the close genetic relationship between the granite and the mineralized skarn, and the short duration of the ore depositional processes normally seen for porphyry systems (e.g., Sillitoe and Mortensen 2010).

IMPLICATIONS

The discovery of abundant hydrothermal zircon and baddeleyite in iron skarns from the Tengtie deposit has important implications for skarnization. Key conclusions from our study are that Zr was both mobilized and readily deposited as baddeleyite or zircon during different stages of skarnization. Although the fluids for skarnization are commonly assumed to be Si-saturated (Meinert et al. 2005), our results show that there was a period of low Si activity relative to original magmatic-hydrothermal fluids due to the formation of pyroxene and garnet during prograde skarnization, which was responsible for the growth of baddeleyite. During the retrograde stage, the growth of zircon was accompanied by mineralization events until a relatively low temperature was reached. This process may be common in skarns characterized by high F activities and associated Zr sources.

Determining the absolute duration of magmatic-hydrothermal mineralization events is one of the key questions in geological studies (Meinert et al. 2005; Chiaradia et al.

2013). Ore depositional processes typically span time ranges from tens to a few hundred thousand years constrained by different isotopic dating systems (e.g., Sillitoe and Mortensen 2010; Chelle-Michou et al. 2015). Although it is difficult to assess the uncertainty of different methods (Chiaradia et al. 2013), currently, the precision of U-Pb dating of zircon can be better than 0.1 % (e.g., Slama et al. 2008). The results from this study, suggest that the skarnization could occur over several million years. In the future, the precision in dating these processes should improve due to continued development in better instrumentation. Hence, acquisition of reliable ages for hydrothermal zircon and baddeleyite, from both prograde and retrograde skarns, may soon become possible, thus providing a better understanding of the magmatic-hydrothermal mineralization processes.

ACKNOWLEDGMENTS

We thank Xiaosong Nie of Chinese Academy of Sciences, and Kencer Ho and Rory Chan of the BMI Technical Consulting (Resources) Limited, Hong Kong, for their assistance in the field. Yazhou Tian of Guizhou University and staffs of associated laboratories are thanked for their help in sample analyses. Special thanks are sent to Paul Robinson of Dalhousie University, Jianfeng Gao of Chinese Academy of Sciences, Kwan-Nan Pang of Academia Sinica, Chris McFariane of University of New Brunswick, Don Davis of University of Toronto, and Xuran Zuo of The University of Hong Kong, for their constructive suggestions and support. Also, we sincerely thank Daniel Harlov and two anonymous reviewers for providing very thorough suggestions. This research was financially supported by HKU CRCG Small Project Funding (201309176142) and SEG Hugh E. McKinstry Fund 2014.

REFERENCES CITED

Ague, J.J. (1994) Mass transfer during Barrovian metamorphism of pelites, south-central Connecticut. I: Evidence for changes in composition and volume. American Journal of Science, 294, 989-1057.

Ague, J.J. (2003) Fluid infiltration and transport of major, minor, and trace elements during regional metamorphism of carbonate rocks, Wepawaug Schist, Connecticut, USA. American Journal of Science, 303, 753-816.

Ague, J.J. (2011) Extreme channelization of fluid and the problem of element mobility during Barrovian metamorphism. American Mineralogist, 96, 333-352.

Bebout, G.E., Ryan, J.G., Leeman, W.P., and Bebout, A.E. (1999) Fractionation of trace elements by subduction-zone metamorphism - effect of convergent-margin thermal evolution. Earth and Planetary Science Letters, 171, 63-81.

Bodnar, R.J. (1994) Synthetic fluid inclusions: XII. The system H2O-NaCl. Experimental determination of the halite liquidus and isochores for a 40 wt% NaCl solution. Geochimica et Cosmochimica Acta, 58, 1053-1063.

Breeding, C.M., Ague, J.J., and Bröcker, M. (2004) Fluid–metasedimentary rock interactions in subduction-zone mélange: implications for the chemical composition of arc magmas. Geology, 32, 1041-1044.

Cavosie, A.J., Valley, J.W., and Wilde, S.A. (2005) Magmatic delta O-18 in 4400-3900 Ma detrital zircons: A record of the alteration and recycling of crust in the Early Archean. Earth and Planetary Science Letters, 235, 663-681.

509 Chelle-Michou, C., Chiaradia, M., Selby, D., Ovtcharova, M., and Spikings, R.A. (2015)
510 High-resolution geochronology of the Coroccohuayco porphyry-skarn deposit,
511 Peru: A rapid product of the Incaic Orogeny. Economic Geology, 110, 423-443.
512 Chen, D.Z., Tucker, M.E., Jiang, M.S., and Zhu, J.Q. (2001) Long-distance correlation
513 between tectonic-controlled, isolated carbonate platforms by cyclostratigraphy
514 and sequence stratigraphy in the Devonian of South China. Sedimentology, 48,
515 57-78.
516 Chen, J.F., and Jahn, B.M. (1998) Crustal evolution of southeastern China: Nd and Sr
517 isotopic evidence. Tectonophysics, 284, 101-133.
518 Cheng, S.B., Fu, J.M., Xu, D.M., Chen, X.Q., Ma, L.-Y., Wang, X.D., and Pang, Y.C.
519 (2009) Zircon SHRIMP U-Pb dating and geochemical characteristics of Daning
520 batholith in northeast Guangxi. Geology in China, 36, 1278-1288.
521 Chiaradia, M., Schaltegger, U., Spikings, R., Wotzlaw, J.F., and Ovtcharova, M. (2013)
522 How accurately can we date the duration of magmatic-hydrothermal events in
523 porphyry systems?-An invited paper. Economic Geology, 108, 565-584.
524 Ciobanu, C.L., and Cook, N.J. (2004) Skarn textures and a case study: the Ocna de Fier-
525 Dognecea orefield, Banat, Romania. Ore Geology Reviews, 24, 315-370.
526 Davidson, A., and Van Breemen, O. (1988) Baddeleyite-zircon relationships in coronitic
527 metagabbro, Grenville Province, Ontario: implications for geochronology.
528 Contributions to Mineralogy and Petrology, 100, 291-299.
529 Dempster, T.J., Hay, D.C., and Bluck, B.J. (2004) Zircon growth in slate. Geology, 32,
530 221-224.

Deng, X.-D., Li, J.-W., and Wen, G. (2015) U-Pb geochronology of hydrothermal zircons from the early Cretaceous iron skarn deposits in the Handan-Xingtai district, North China craton. Economic Geology, 110, 2159-2180.

Drummond, M.S., Defant, M.J., and Kepezhinskas, P.K. (1996) Petrogenesis of slab-derived trondhjemite-tonalite-dacite/adakite magmas. Geological Society of America Special Papers, 315, 205-215.

Einaudi, M.T., Meinert, L.D., and Newberry, R.J. (1981) Skarn deposits. Economic Geology, 75, 317-391.

Ernst, R.E., and Buchan, K.L. (2003) Recognizing mantle plumes in the geological record. Annual Review of Earth and Planetary Sciences, 31, 469-523.

Floyd, P.A., and Winchester, J.A. (1975) Magma type and tectonic setting discrimination using immobile elements. Earth and Planetary Science Letters, 27, 211-218.

Gao, J.F., Ling, H.F., Sheng, W.Z., Lu, J.J., Zhang, M., Huang, G.L., and Tan, Z.Z. (2005) Geochemistry and petrogenesis of Lianyang granite composite, west Guangdong province. Acta Petrologica Sinica, 21, 1645-1656.

Gaspar, M., Knaack, C., Meinert, L.D., and Moretti, R. (2008) REE in skarn systems: A LA-ICP-MS study of garnets from the Crown Jewel gold deposit. Geochimica et Cosmochimica Acta, 72, 185-205.

Geisler, T., Rashwan, A.A., Rahn, M.K.W., Poller, U., Zwingmann, H., Pidgeon, R.T., Schleicher, H., and Tomaschek, F. (2003) Low-temperature hydrothermal alteration of natural metamict zircons from the Eastern Desert, Egypt. Mineralogical Magazine, 67, 485-508.

553 Geisler, T., Schaltegger, U., and Tomaschek, F. (2007) Re-equilibration of zircon in
554 aqueous fluids and melts. Elements, 3, 43-50.
555 Geisler, T., Ulonska, M., Schleicher, H., Pidgeon, R.T., and van Bronswijk, W. (2001)
556 Leaching and differential recrystallization of metamict zircon under experimental
557 hydrothermal conditions. Contributions to Mineralogy and Petrology, 141, 53-65.
558 Gieré, R. (1986) Zirconolite, allanite and hoegbomite in a marble skarn from the Bergell
559 contact aureole - Implications for mobility of Ti, Zr and REE. Contributions to
560 Mineralogy and Petrology, 93, 459-470.
561 Gieré, R., and Williams, C.T. (1992) REE-bearing minerals in a Ti-rich vein from the
562 Adamello contact aureole (Italy). Contributions to Mineralogy and Petrology,
563 112, 83-100.
564 Haas, J.R., Shock, E.L., and Sassani, D.C. (1995) Rare earth elements in hydrothermal
565 systems: estimates of standard partial molal thermodynamic properties of aqueous
566 complexes of the rare earth elements at high pressures and temperatures.
567 Geochimica et Cosmochimica Acta, 59, 4329-4350.
568 He, Z., Huang, F., Yu, H., Xiao, Y., Wang, F., Li, Q., Xia, Y., and Zhang, X. (2015) A
569 flux-free fusion technique for rapid determination of major and trace elements in
570 silicate rocks by LA-ICP-MS. Geostandards and Geoanalytical Research, 40, 5-
571 27.
572 Hoskin, P.W.O. (2005) Trace-element composition of hydrothermal zircon and the
573 alteration of Hadean zircon from the Jack Hills, Australia. Geochimica et
574 Cosmochimica Acta, 69, 637-648.

575 Hu, R.Z., and Zhou, M.F. (2012) Multiple Mesozoic mineralization events in South
576 China-an introduction to the thematic issue. Mineralium Deposita, 47, 579-588.
577 Ismail, R., Ciobanu, C.L., Cook, N.J., Teale, G.S., Giles, D., Mumm, A.S., and Wade, B.
578 (2014) Rare earths and other trace elements in minerals from skarn assemblages,
579 Hillside iron oxide-copper-gold deposit, Yorke Peninsula, South Australia. Lithos,
580 184, 456-477.
581 Keppler, H. (1993) Influence of fluorine on the enrichment of high field strength trace
582 elements in granitic rocks. Contributions to Mineralogy and Petrology, 114, 479-
583 488.
584 Kerrich, R., and King, R. (1993) Hydrothermal Zircon and Baddeleyite in Val-Dor
585 Archean Mesothermal Gold Deposits - Characteristics, Compositions, and Fluid-
586 Inclusion Properties, with Implications for Timing of Primary Gold
587 Mineralization. Canadian Journal of Earth Sciences, 30, 2334-2351.
588 Kirkland, C.L., Whitehouse, M.J., and Slagstad, T. (2009) Fluid-assisted zircon and
589 monazite growth within a shear zone: a case study from Finnmark, Arctic
590 Norway. Contributions to Mineralogy and Petrology, 158, 637-657.
591 Kusiak, M.A., Dunkley, D.J., Słaby, E., Martin, H., and Budzyń, B. (2009) Sensitive
592 high-resolution ion microprobe analysis of zircon reequilibrated by late magmatic
593 fluids in a hybridized pluton. Geology, 37, 1063-1066.
594 Lawrie, K.C., Mernagh, T.P., Ryan, C.G., van Achterbergh, E., and Black, L.P. (2007)
595 Chemical fingerprinting of hydrothermal zircons: An example from the
596 Gidginbung high sulphidation Au-Ag-(Cu) deposit, New South Wales, Australia.
597 Proceedings of the Geologists Association, 118, 37-46.

598 Li, X.H., Liu, Y., Li, Q.L., Guo, C.H., and Chamberlain, K.R. (2009) Precise
599 determination of Phanerozoic zircon Pb/Pb age by multicollector SIMS without
600 external standardization. Geochemistry, Geophysics, Geosystems, 10, 1525-2027.
601 Li, X.H., Long, W.G., Li, Q.L., Liu, Y., Zheng, Y.F., Yang, Y.H., Chamberlain, K.R.,
602 Wan, D.F., Guo, C.H., and Wang, X.C. (2010) Penglai zircon megacrysts: a
603 potential new working reference material for microbeam determination of Hf-O
604 isotopes and U-Pb age. Geostandards and Geoanalytical Research, 34, 117-134.
605 Linnen, R.L., Samson, I.M., Williams-Jones, A.E., and Chakhmouradian, A.R. (2014).
606 Geochemistry of the rare-earth element, Nb, Ta, Hf, and Zr deposits. In Turekian,
607 H.D.H.K. Ed., Treatise on Geochemistry (Second Edition), p. 543-568, Elsevier,
608 Oxford.
609 Liu, Y.S., Gao, S., Hu, Z.C., Gao, C.G., Zong, K.Q., and Wang, D.B. (2010) Continental
610 and oceanic crust recycling-induced melt-peridotite interactions in the Trans-
611 North China Orogen: U-Pb dating, Hf isotopes and trace elements in zircons from
612 mantle xenoliths. Journal of Petrology, 51, 537-571.
613 Mao, J.W., Cheng, Y.B., Chen, M.H., and Pirajno, F. (2013) Major types and time-space
614 distribution of Mesozoic ore deposits in South China and their geodynamic
615 settings. Mineralium Deposita, 48, 267-294.
616 McDonough, W.F., and Sun, S.S. (1995) The composition of the Earth. Chemical
617 Geology, 120, 223-253.
618 McLaren, A.C., Gerald, J.D.F., and Williams, I.S. (1994) The microstructure of zircon
619 and its influence on the age determination from Pb/U isotopic ratios measured by
620 ion microprobe. Geochimica et Cosmochimica Acta, 58, 993-1005.

621 Meinert, L., Dipple, G., and Nicolescu, S. (2005) World skarn deposits. Economic
622 Geology, 100, 299-336.
623 Mezger, K., and Krogstad, E.J. (1997) Interpretation of discordant U-Pb zircon ages: An
624 evaluation. Journal of Metamorphic Geology, 15, 127-140.
625 Migdisov, A.A., and Williams-Jones, A.E. (2007) An experimental study of the solubility
626 and speciation of neodymium (III) fluoride in F-bearing aqueous solutions.
627 Geochimica et Cosmochimica Acta, 71, 3056-3069.
628 Migdisov, A.A., Williams-Jones, A.E., van Hinsberg, V., and Salvi, S. (2011) An
629 experimental study of the solubility of baddeleyite (ZrO2) in fluoride-bearing
630 solutions at elevated temperature. Geochimica et Cosmochimica Acta, 75, 7426-
631 7434.
632 Migdisov, A.A., Williams-Jones, A.E., and Wagner, T. (2009) An experimental study of
633 the solubility and speciation of the Rare Earth Elements (III) in fluoride-and
634 chloride-bearing aqueous solutions at temperatures up to 300 ºC. Geochimica et
635 Cosmochimica Acta, 73, 7087-7109.
636 Moine, B., Ramambazafy, A., Rakotondrazafy, M., Ravololomiandrinarivo, B., Cuney,
637 M., and De Parseval, P. (1998) The role of fluor-rich fluids in the formation of the
638 thorianite and sapphire deposits from SE Madagascar. Mineralogical Magazine,
639 62, 999-1000.
640 Mursic, Z., Vogt, T., Boysen, H., and Frey, F. (1992) Single-crystal neutron diffraction
641 study of metamict zircon up to 2000 K. Journal of applied crystallography, 25,
642 519-523.

643 Nasdala, L., Beran, A., Libowitzky, E., and Wolf, D. (2001) The incorporation of
644 hydroxyl groups and molecular water in natural zircon (ZrSiO4). American
645 Journal of Science, 301, 831-857.
646 Nesbitt, R.W., Pascual, E., Fanning, C.M., Toscano, M., Saez, R., and Almodovar, G.R.
647 (1999) U-Pb dating of stockwork zircons from the eastern Iberian Pyrite Belt.
648 Journal of the Geological Society, 156, 7-10.
649 Pearce, J.A. (1996) Sources and settings of granitic rocks. Episodes, 19, 120-125.
650 Pearce, J.A. (2008) Geochemical fingerprinting of oceanic basalts with applications to
651 ophiolite classification and the search for Archean oceanic crust. Lithos, 100, 14-
652 48.
653 Pearce, J.A., and Cann, J.R. (1973) Tectonic setting of basic volcanic rocks determined
654 using trace element analyses. Earth and Planetary Science Letters, 19, 290-300.
655 Pelleter, E., Cheilletz, A., Gasquet, D., Mouttaqi, A., Annich, M., El Hakour, A., Deloule,
656 E., and Feraud, G. (2007) Hydrothermal zircons: A tool for ion microprobe U-Pb
657 dating of gold mineralization (Tamlalt-Menhouhou gold deposit Morocco).
658 Chemical Geology, 245, 135-161.
659 Penniston-Dorland, S.C., and Ferry, J.M. (2008) Element mobility and scale of mass
660 transport in the formation of quartz veins during regional metamorphism of the
661 Waits River Formation, east-central Vermont. American Mineralogist, 93, 7-21.
662 Pettke, T., Audetat, A., Schaltegger, U., and Heinrich, C.A. (2005) Magmatic-to-
663 hydrothermal crystallization in the W-Sn mineralized Mole Granite (NSW,
664 Australia) - Part II: Evolving zircon and thorite trace element chemistry. Chemical
665 Geology, 220, 191-213.

Pidgeon, R.T., Nemchin, A.A., and Cliff, J. (2013) Interaction of weathering solutions with oxygen and U-Pb isotopic systems of radiation-damaged zircon from an Archean granite, Darling Range Batholith, Western Australia. Contributions to Mineralogy and Petrology, 166, 511-523.

Rizvanova, N.G., Levchenkov, O.A., Belous, A.E., Bezmen, N.I., Maslenikov, A.V., Komarov, A.N., Makeev, A.F., and Levskiy, L.K. (2000) Zircon reaction and stability of the U-Pb isotope system during interaction with carbonate fluid: experimental hydrothermal study. Contributions to Mineralogy and Petrology, 139, 101-114.

Rubenach, M. (2013). Structural controls of metasomatism on a regional scale. In Harlov, D.E. and Håkon, A. Eds., Metasomatism and the chemical transformation of rock, p. 93-140, Springer, Berlin Heidelberg.

Rubin, J.N., Henry, C.D., and Price, J.G. (1989) Hydrothermal zircons and zircon overgrowths, Sierra-Blanca Peaks, Texas. American Mineralogist, 74, 865-869.

Rubin, J.N., Henry, C.D., and Price, J.G. (1993) The mobility of zirconium and other immobile elements during hydrothermal alteration. Chemical Geology, 110, 29-47.

Salvi, S., Fontan, F., Monchoux, P., Williams-Jones, A., and Moine, B. (2000) Hydrothermal mobilization of high field strength elements in alkaline igneous systems: evidence from the Tamazeght Complex (Morocco). Economic Geology, 95, 559-576.

Salvi, S., and Williams-Jones, A.E. (1996) The role of hydrothermal processes in concentrating high-field strength elements in the Strange Lake peralkaline

689 complex, northeastern Canada. Geochimica et Cosmochimica Acta, 60, 1917-
690 1932.
691 Sillitoe, R.H., and Mortensen, J.K. (2010) Longevity of porphyry copper formation at
692 Quellaveco, Peru. Economic Geology, 105, 1157-1162.
693 Slama, J., Kosler, J., Condon, D.J., Crowley, J.L., Gerdes, A., Hanchar, J.M., Horstwood,
694 M.S.A., Morris, G.A., Nasdala, L., Norberg, N., and others (2008) Plesovice
695 zircon - A new natural reference material for U-Pb and Hf isotopic microanalysis.
696 Chemical Geology, 249, 1-35.
697 Smith, M.P., Henderson, P., Jeffries, T.E.R., Long, J., and Williams, C.T. (2004) The rare
698 earth elements and uranium in garnets from the Beinn an Dubhaich Aureole,
699 Skye, Scotland, UK: constraints on processes in a dynamic hydrothermal system.
700 Journal of Petrology, 45, 457-484.
701 Söderlund, U., Hellström, F.A., and Kamo, S.L. (2008) Geochronology of high-pressure
702 mafic granulite dykes in SW Sweden: tracking the P-T-t path of metamorphism
703 using Hf isotopes in zircon and baddeleyite. Journal of Metamorphic Geology, 26,
704 539-560.
705 Solar, G.S., and Brown, M. (2001) Petrogenesis of migmatites in Maine, USA: possible
706 source of peraluminous leucogranite in plutons? Journal of Petrology, 42, 789-
707 823.
708 Tang, G.-Q., Li, X.-H., Li, Q.-L., Liu, Y., Ling, X.-X., and Yin, Q.-Z. (2015)
709 Deciphering the physical mechanism of the topography effect for oxygen isotope
710 measurements using a Cameca IMS-1280 SIMS. Journal of Analytical Atomic
711 Spectrometry, 30, 950-956.

712 Toscano, M., Pascual, E., Nesbitt, R., Almodóvar, G., Sáez, R., and Donaire, T. (2014)
713 Geochemical discrimination of hydrothermal and igneous zircon in the Iberian
714 Pyrite Belt, Spain. Ore Geology Reviews, 56, 301-311.
715 Trail, D., Watson, E.B., and Tailby, N.D. (2011) The oxidation state of Hadean magmas
716 and implications for early Earth's atmosphere. Nature, 480, 79-82.
717 Tropper, P., Manning, C.E., and Harlov, D.E. (2011) Solubility of CePO4 monazite and
718 YPO4 xenotime in H2O and H2O-NaCl at 800 ºC and 1GPa: implications for
719 REE and Y transport during high-grade metamorphism. Chemical Geology, 282,
720 58-66.
721 Tropper, P., Manning, C.E., and Harlov, D.E. (2013) Experimental determination of
722 CePO4 and YPO4 solubilities in H2O-NaF at 800 ºC and 1GPa: implications for
723 rare earth element transport in high‐grade metamorphic fluids. Geofluids, 13,
724 372-380.
725 Valley, J.W. (2003) Oxygen isotopes in zircon. Reviews in Mineralogy and
726 Geochemistry, 53, 343-385.
727 Wang, X.-L., Coble, M.A., Valley, J.W., Shu, X.-J., Kitajima, K., Spicuzza, M.J., and
728 Sun, T. (2014) Influence of radiation damage on Late Jurassic zircon from
729 southern China: Evidence from in situ measurements of oxygen isotopes, laser
730 Raman, U–Pb ages, and trace elements. Chemical Geology, 389, 122-136.
731 White, L.T., and Ireland, T.R. (2012) High-uranium matrix effect in zircon and its
732 implications for SHRIMP U-Pb age determinations. Chemical Geology, 306, 78-
733 91.

734 Whitney, D.L., and Evans, B.W. (2010) Abbreviations for names of rock-forming
735 minerals. American Mineralogist, 95, 185-187.
736 Williams-Jones, A.E., and Migdisov, A.A. (2014) Experimental constraints on the
737 transport and deposition of metals in ore-forming hydrothermal systems. Society
738 of Economic Geologists, 18, 77-96.
739 Williams-Jones, A.E., Migdisov, A.A., and Samson, I.M. (2012) Hydrothermal
740 mobilisation of the rare earth elements–a tale of "ceria" and "yttria". Elements, 8,
741 355-360.
742 Yan, D.P., Zhou, M.F., Song, H.L., Wang, X.W., and Malpas, J. (2003) Origin and
743 tectonic significance of a Mesozoic multi-layer over-thrust system within the
744 Yangtze Block (South China). Tectonophysics, 361, 239-254.
745 Yang, W.-B., Niu, H.-C., Shan, Q., Sun, W.-D., Zhang, H., Li, N.-B., Jiang, Y.-H., and
746 Yu, X.-Y. (2014) Geochemistry of magmatic and hydrothermal zircon from the
747 highly evolved Baerzhe alkaline granite: implications for Zr-REE-Nb
748 mineralization. Mineralium Deposita, 49, 451-470.
749 Yu, J.H., Zhou, X.M., O'Reilly, Y.S., Zhao, L., Griffin, W.L., Wang, R.C., Wang, L.J.,
750 and Chen, X.M. (2005) Formation history and protolith characteristics of
751 granulite facies metamorphic rock in Central Cathaysia deduced from U-Pb and
752 Lu-Hf isotopic studies of single zircon grains. Chinese Science Bulletin, 50, 2080-
753 2089.
754 Zhao, J.H., Zhou, M.F., Yan, D.P., Zheng, J.P., and Li, J.W. (2011) Reappraisal of the
755 ages of Neoproterozoic strata in South China: No connection with the Grenvillian
756 orogeny. Geology, 39, 299-302.

Zhao, W.W., and Zhou, M.-F. (2015) In-situ LA–ICP-MS trace elemental analyses of magnetite: The Mesozoic Tengtie skarn Fe deposit in the Nanling Range, South China. Ore Geology Reviews, 65, 872-883.

Zheng, Y.-F. (1993) Calculation of oxygen isotope fractionation in anhydrous silicate minerals. Geochimica et Cosmochimica Acta, 57, 1079-1079.

Zhou, M.F., Yan, D.P., Kennedy, A.K., Li, Y.Q., and Ding, J. (2002) SHRIMP U-Pb zircon geochronological and geochemical evidence for Neoproterozoic arc-magmatism along the western margin of the Yangtze Block, South China. Earth and Planetary Science Letters, 196, 51-67.

Zhou, X.M., Sun, T., Shen, W.Z., Shu, L.S., and Niu, Y.L. (2006) Petrogenesis of Mesozoic granitoids and volcanic rocks in South China: A response to tectonic evolution. Episodes, 29, 26-33.

771 **FIGURE CAPTIONS**

772

773 **Figure 1**. (**a**) Regional map of South China. (**b**) Location of the Tengtie skarn deposit
774 and distribution of mining sites in the deposit (Zhao and Zhou 2015).

775

776 **Figure 2**. Microscopic images of hydrothermal Type 1 zircon in thin sections from the
777 Tengtie skarn. (**a**)-(**f**) BSE images. (**g**) CL image. (**h**) Transmitted-light image. Mineral
778 name abbreviations (Whitney and Evans 2010): Baddeleyite-Bdy, Calcite-Cal,
779 Cassiterite-Cst, Chlorite-Chl, Diopside-Di, Epidote-Ep, Fluorite-Fl, Magnetite-Mag,
780 Zircon-Zrn.

781

782 **Figure 3**. Microscopic images of the rounded Type 2 zircon separates (**a**)-(**d**), transparent
783 Type 3 zircon separates from the late granitic phase (**e**)-(**h**), and translucent Type 4 zircon
784 separates from early the granitic phase (**i**)-(**p**) separates from Tengtie deposit. (**a**), (**e**), (**i**)
785 BSE image. (**b**), (**f**), (**j**) CL image. (**c**), (**g**), (**k**) Reflected-light image. (**d**), (**h**), (**l**)
786 Transmitted-light image. (**m**), (**n**), (**o**), (**p**) EDS elemental mapping images.

787

788 **Figure 4**. Oxygen isotope ranges of zircon from the Tengtie deposit.

789

790 **Figure 5**. SIMS U–Pb concordia age plots for zircons from the Tengtie skarn deposit. (**a**)
791 Hydrothermal Type 1b zircons from the retrograde stage of the Tengtie skarns. (**b**)
792 Detrital Type 2 zircons from the Tengtie skarns. (**c**) Magmatic Type 3 zircons from the
793 late granitic phase of the Mesozoic pluton.

794 **Figure 6**. (**a**), (**b**) Chondrite-normalized zircon REE patterns. (**c**) $(Sm/La)_N$ vs La
795 diagram. The shadowed field is defined by Hoskin (2005), and the dashed straight line by
796 (Kirkland et al. 2009). Chondrite normalizing values are from McDonough and Sun
797 (1995).
798
799 **Figure 7**. Spider diagrams of chondrite-normalized trace elements from skarn minerals
800 from both early and late prograde stages. (**a**) Garnet. (**b**) Diopside. Chondrite normalizing
801 values from McDonough and Sun (1995).
802
803 **Figure 8**. Histogram of homogenization temperatures of fluid inclusions in hydrothermal
804 calcite coexisting with hydrothermal Type 1b zircon from the Tengtie skarn.
805
806 **Figure 9**. Mobilization of Zr and formation process for the baddeleyite and zircon in the
807 Tengtie deposit. The paragenetic sequence of alteration and mineralization in the Tengtie
808 deposit is deduced from the results in this study and data from (Zhao and Zhou 2015). (**a**)
809 Fluorine-rich hydrothermal fluids evolved from the late granite. (**b**) Magmatic-
810 hydrothermal fluids interacted with carbonates to form HSFE-bearing prograde skarn
811 minerals, such as diopside. (**c**) Relatively Si-depleted fluids deposited baddeleyite-zircon
812 intergrowth with fluorite in the pores of the prograde skarn minerals. (**d**) Retrograde
813 alteration caused release of Zr and Sn from HSFE-bearing skarn minerals to form zircon
814 and cassiterite with retrograde skarn minerals and magnetite. (**e**) Annealing and leaching
815 of high-U zircon under low temperature. Mineral name abbreviations (Whitney and

816 Evans 2010): Baddeleyite-Bdy, Calcite-Cal, Cassiterite-Cst, Chlorite-Chl, Diopside-Di,
817 Epidote-Ep, Fluorite-Fl, Garnet-Gt, Magnetite-Mag, Zircon-Zrn.
818
819
820
821
822

Table 1 EMPA data (wt%) for zircon and baddeleyite

	SiO_2	CaO	P_2O_5	Y_2O_3	ZrO_2	La_2O_3	Ce_2O_3	Eu_2O_3	Sm_2O_3	Lu_2O_3	HfO_2	TiO_2	UO_2	Total
Type 1 zircon														
TT14-05-1	32.5	-	-	-	65.1	0.10	0.13	0.18	0.09	-	1.06	0.02	0.56	99.68
TT14-05-2	32.6	0.03	-	0.01	63.9	-	0.27	-	-	-	0.72	0.06	0.35	98.00
TT14-05-3	32.4	0.04	-	-	64.8	0.23	0.24	-	0.02	0.23	0.58	0.02	0.58	99.17
TT14-05-4	32.3	-	-	-	64.8	-	0.37	-	0.15	-	1.05	0.01	0.12	98.84
TT14-05-5	32.1	0.06	-	-	62.8	0.25	0.49	0.01	0.10	-	1.15	0.03	0.27	97.30
Type 3 zircon														
TT14-1617-1	32.4	0.17	0.30	0.26	63.6	0.13	0.02	-	-	0.12	1.24	0.03	0.09	98.36
TT14-1617-2	32.7	0.02	-	-	64.6	0.10	0.03	-	-	-	1.14	0.06	-	98.71
TT14-34-1	32.4	0.03	0.07	0.26	64.6	-	0.08	-	-	-	0.77	0.03	0.04	98.23
TT14-34-2	33.1	-	0.05	0.05	64.1	-	0.02	0.12	0.21	-	1.50	-	0.03	99.11
Type 4 zircon														
TT14-13-1	32.4	0.36	0.67	3.49	48.8	0.06	-	-	-	0.39	1.42	0.02	8.04	95.73
TT14-13-3	30.5	0.01	0.23	1.90	56.6	-	0.33	0.04	0.05	0.48	1.96	0.03	5.66	97.71
TT14-13-2	32.1	0.18	0.47	2.47	54.7	-	0.03	0.02	-	0.25	1.54	0.07	4.93	96.71
TT14-13-6	30.8	-	0.35	1.95	56.5	0.12	0.13	0.03	-	0.27	2.77	0.01	4.57	97.50
TT14-13-5	29.2	1.22	0.75	2.75	52.2	-	0.06	0.03	-	0.44	3.03	0.08	5.30	95.02
TT14-13-4	32.5	3.21	0.63	2.71	49.5	-	0.05	-	0.10	0.32	2.85	-	4.75	96.59
TT14-13-7	30.0	-	1.11	3.56	52.8	-	-	0.08	-	0.30	2.87	0.03	5.58	96.25
TT14-13-8	31.6	0.24	0.94	2.91	52.2	-	0.27	-	-	0.43	2.66	-	5.26	96.58
TT14-13-9	31.0	0.01	0.33	1.84	56.8	-	0.02	-	-	0.35	2.59	-	4.07	96.97
TT14-13-10	32.1	0.09	0.26	1.66	55.1	-	-	0.18	-	0.06	2.62	0.01	4.53	96.57
Baddeleyite														
TT14-04-BD2	-	-	-	-	97.2	0.15	-	-	0.04	0.15	0.48	0.05	-	98.07
TT14-04-BD3	-	-	-	-	98.7	0.11	-	-	-	0.12	1.44	0.01	-	100.42
TT14-04-BD4	-	-	-	-	98.6	-	-	-	0.12	-	1.39	-	-	100.10

Note: "-": below detection limit of 0.01 wt%.

823

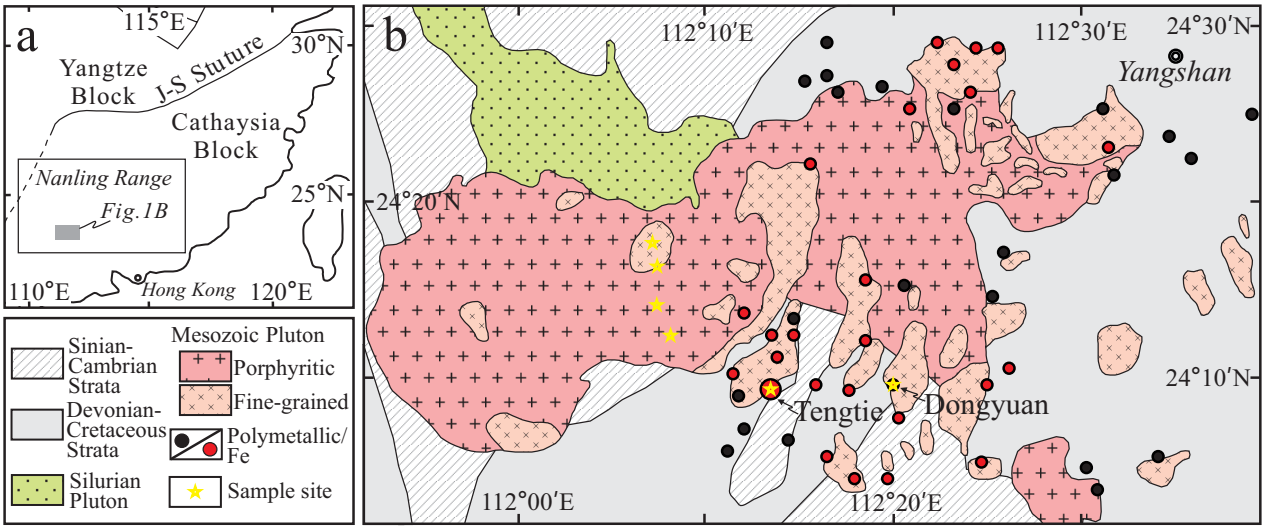
a
115°E
30°N
Yangtze Block
J-S Stuture
Cathaysia Block
Nanling Range
Fig.1B
25°N
110°E
Hong Kong
120°E
Sinian-Cambrian Strata
Devonian-Cretaceous Strata
Silurian Pluton
Mesozoic Pluton
Porphyritic
Fine-grained
Polymetallic/ Fe
Sample site
b
112°10′E
112°30′E
24°30′N
Yangshan
24°20′N
24°10′N
Tengtie
Dongyuan
112°00′E
112°20′E

Figure 1

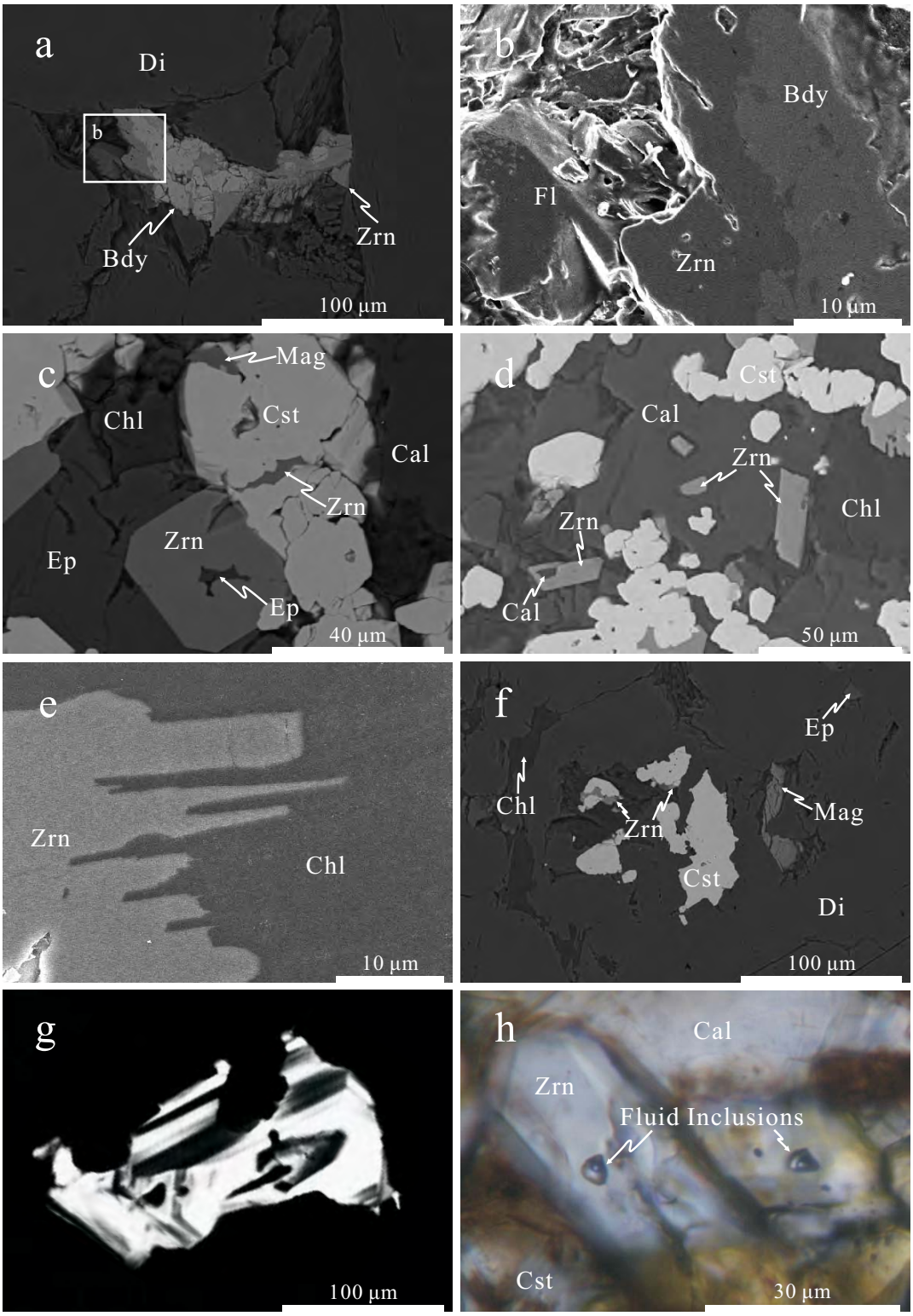
a
Di
b
Zrn
Bdy
100 µm
b
Bdy
Fl
Zrn
10 µm
c
Mag
Chl
Cst
Cal
Zrn
Zrn
Ep
Ep
40 µm
d
Cst
Cal
Zrn
Zrn
Chl
Cal
50 µm
e
Zrn
Chl
10 µm
f
Ep
Chl
Zrn
Mag
Cst
Di
100 µm
g
100 µm
h
Cal
Zrn
Fluid Inclusions
Cst
30 µm

Figure 2

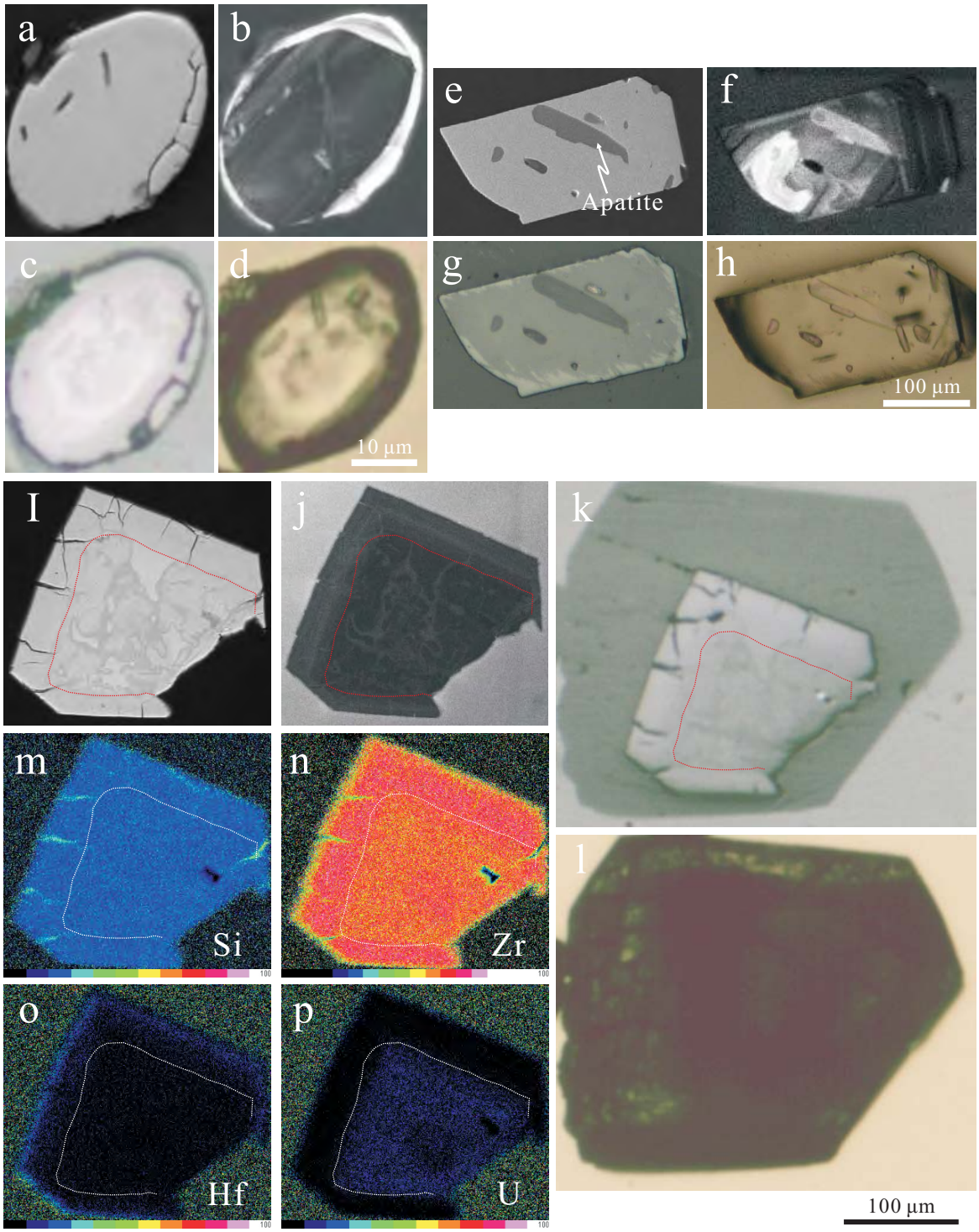

Figure 3

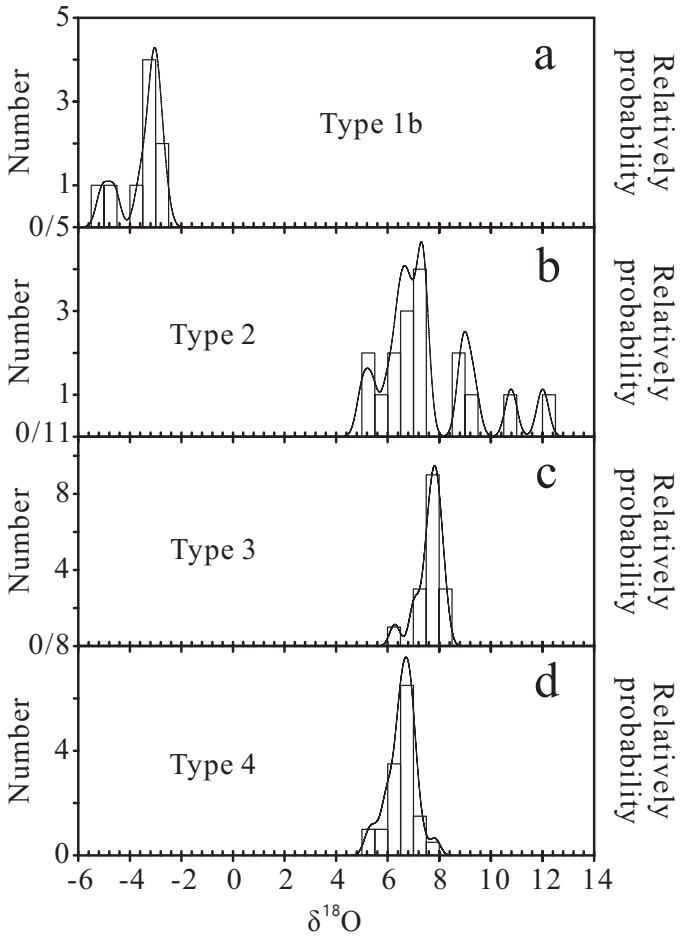
a
Type 1b
b
Type 2
c
Type 3
d
Type 4
Number
Relatively probability
5
3
1
0/5
0/11
8
4
0/8
0
-6 -4 -2 0 2 4 6 8 10 12 14
δ18O

Figure 4

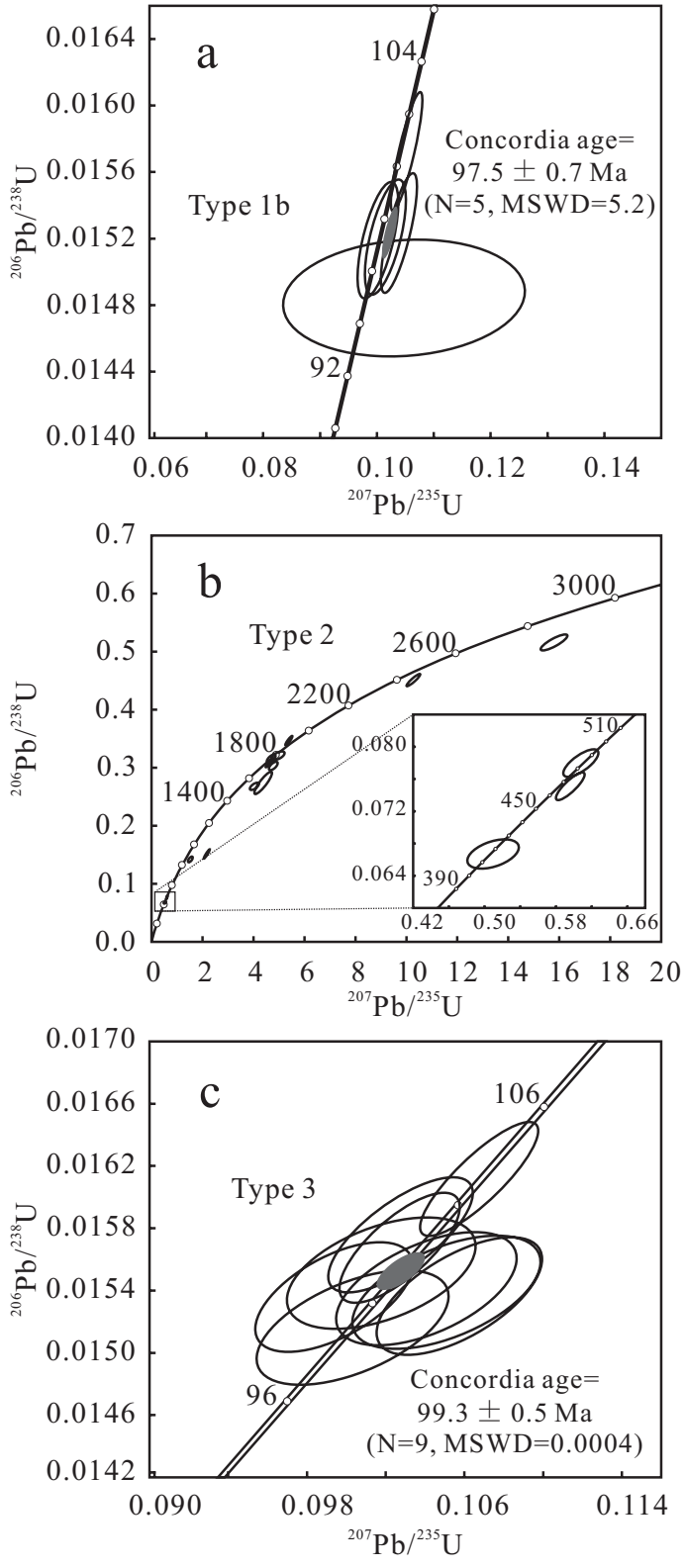
a
104
92
Type 1b
Concordia age=
97.5 ± 0.7 Ma
(N=5, MSWD=5.2)
0.0164
0.0160
0.0156
0.0152
0.0148
0.0144
0.0140
0.06
0.08
0.10
0.12
0.14
206Pb/238U
207Pb/235U
b
Type 2
3000
2600
2200
1800
1400
510
450
390
0.080
0.072
0.064
0.42
0.50
0.58
0.66
0.7
0.6
0.5
0.4
0.3
0.2
0.1
0.0
0
2
4
6
8
10
12
14
16
18
20
206Pb/238U
207Pb/235U
c
106
96
Type 3
Concordia age=
99.3 ± 0.5 Ma
(N=9, MSWD=0.0004)
0.0170
0.0166
0.0162
0.0158
0.0154
0.0150
0.0146
0.0142
0.090
0.098
0.106
0.114
206Pb/238U
207Pb/235U

Figure 5

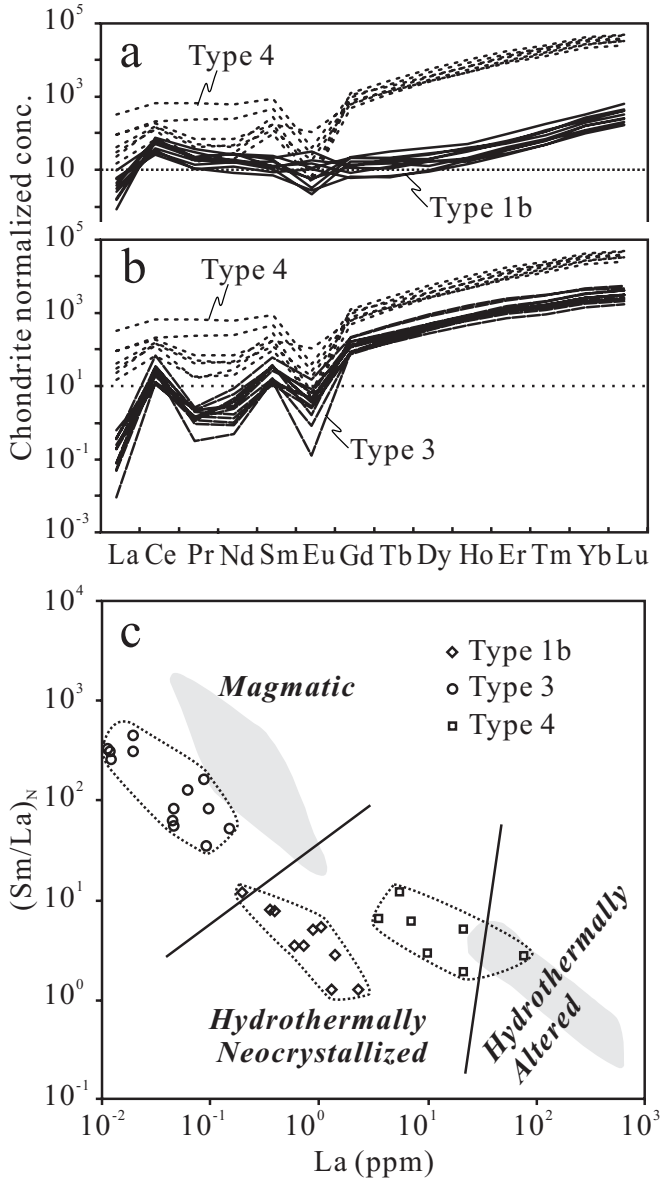
a
Type 4
Type 1b
b
Type 4
Type 3
Chondrite normalized conc.
La Ce Pr Nd Sm Eu Gd Tb Dy Ho Er Tm Yb Lu
c
Type 1b
Type 3
Type 4
Magmatic
Hydrothermally Neocrystallized
Hydrothermally Altered
(Sm/La)N
La (ppm)

Figure 6

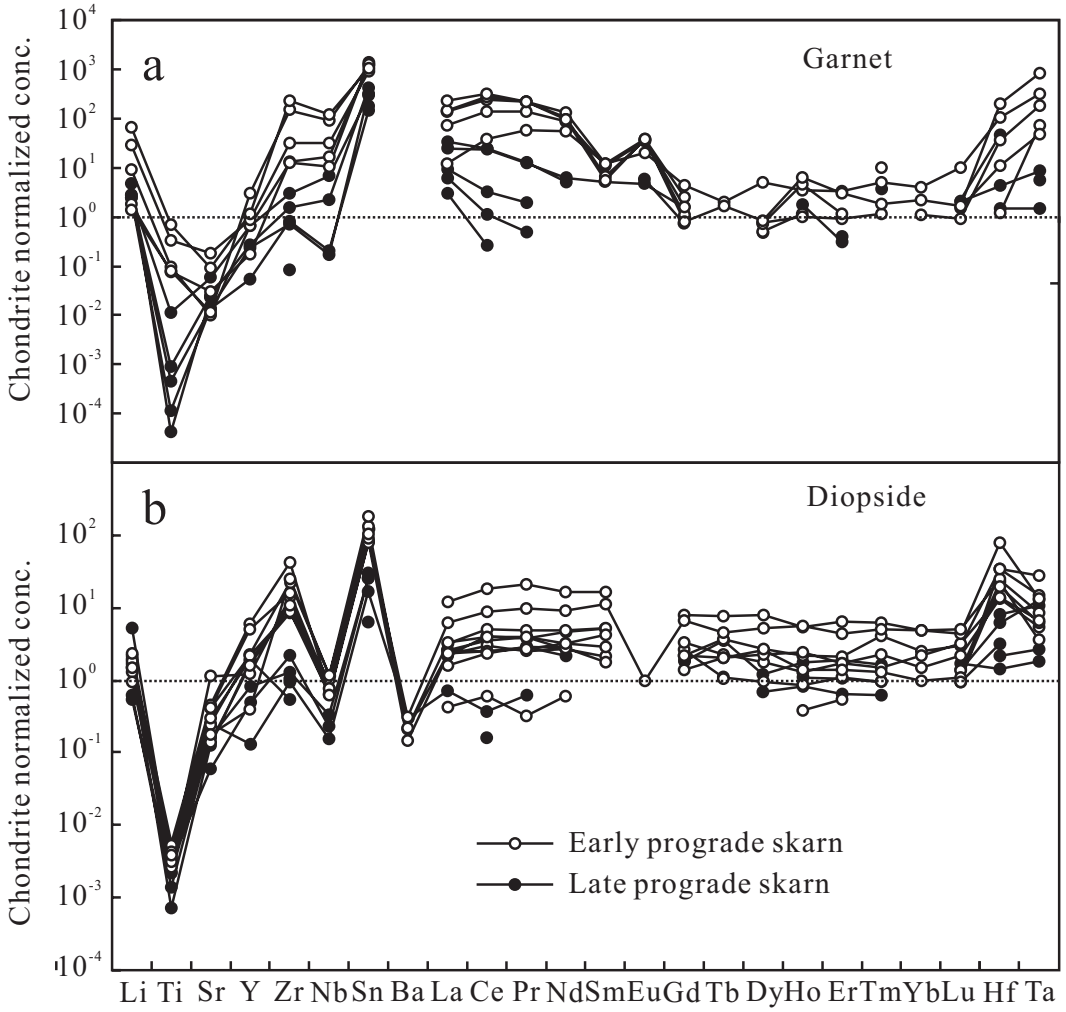
a
Garnet
b
Diopside
Chondrite normalized conc.
Chondrite normalized conc.
Early prograde skarn
Late prograde skarn
Li Ti Sr Y Zr Nb Sn Ba La Ce Pr Nd Sm Eu Gd Tb Dy Ho Er Tm Yb Lu Hf Ta

Figure 7

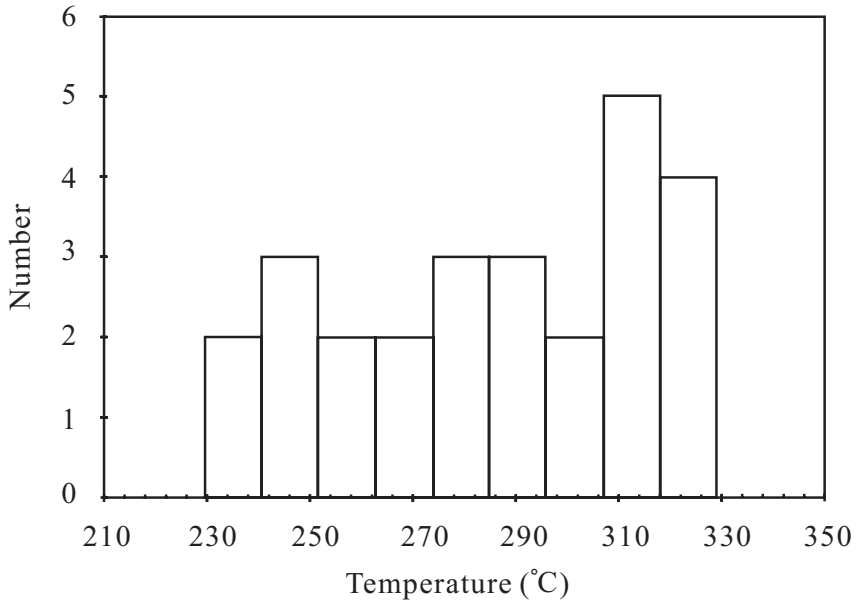

Figure 8

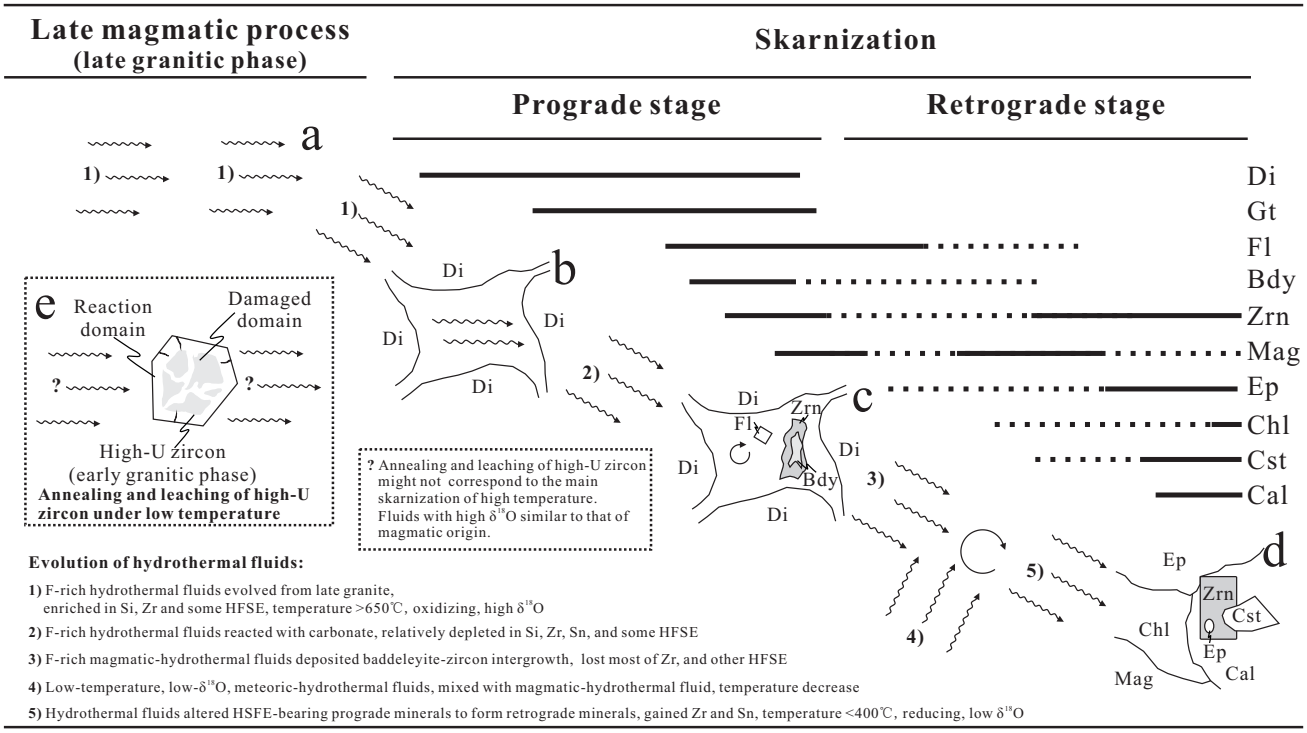
Late magmatic process
(late granitic phase)
Skarnization
Prograde stage
Retrograde stage
a
1)
1)
1)
b
Di
Di
Di
Di
2)
c
Di
Fl
Zrn
Di
Di
Bdy
Di
3)
4)
5)
d
Ep
Zrn
Cst
Chl
Ep
Mag
Cal
Di
Gt
Fl
Bdy
Zrn
Mag
Ep
Chl
Cst
Cal
e
Reaction domain
Damaged domain
?
?
High-U zircon
(early granitic phase)
Annealing and leaching of high-U zircon under low temperature
? Annealing and leaching of high-U zircon might not correspond to the main skarnization of high temperature. Fluids with high δ18O similar to that of magmatic origin.
Evolution of hydrothermal fluids:
1) F-rich hydrothermal fluids evolved from late granite, enriched in Si, Zr and some HFSE, temperature >650℃, oxidizing, high δ18O
2) F-rich hydrothermal fluids reacted with carbonate, relatively depleted in Si, Zr, Sn, and some HFSE
3) F-rich magmatic-hydrothermal fluids deposited baddeleyite-zircon intergrowth, lost most of Zr, and other HFSE
4) Low-temperature, low-δ18O, meteoric-hydrothermal fluids, mixed with magmatic-hydrothermal fluid, temperature decrease
5) Hydrothermal fluids altered HSFE-bearing prograde minerals to form retrograde minerals, gained Zr and Sn, temperature <400℃, reducing, low δ18O

Figure 9